Supplementary Material of

Secure Multi-Hop Relaying in Large-Scale Space-Air-Ground-Sea Integrated Networks

Contents

A. Related Works

Recent studies have explored diverse approaches to secure communication in SAGSIN. We survey both general physical-layer security strategies and secure routing approaches in the broader context of NTNs, including LEO and HAP networks. These related works are summarized in Table. 1.

A.1. Secure Communications in SAGSINs

[11] proposes an aerial bridge scheme using UAVs to form secure tunnels and reduce the eavesdropping footprint. [12] enhances secrecy rate via a joint UAV deployment and power allocation using successive convex approximation to decouple complex multi-layer constraints, and [13] further enhances security by optimizing UAV trajectory and power with a hybrid FSO/RF scheme that mitigates RF vulnerabilities through optical satellite links. Similarly, [14] combines UAV-assisted non-orthogonal multiple access with cooperative jamming to counter both internal and external eavesdropping threats in SAGINs. [15] proposes a label□free deep learning framework that dynamically selects access strategies to maximize sum secrecy rate. [16] optimizes HAPs trajectories and beamforming by employing a generative AI-based DRL framework for proactive adaptation and improved secrecy energy efficiency under dynamic channel changes.

These studies have contributed to improving various secrecy utilities in small-scale SAGSINs with less than two-hops under the perfect knowledge of Eves. However, it is essential to investigate wide-area multi-hop communications under imperfect knowledge of Eve' s channel, as SAGSINs are fundamentally intended to enable ubiquitous global connectivity.

A.2. Secure Routing in NTNs

[25] presents a hybrid SDN architecture with hierarchical control to enable secure and QoS-aware routing in SAGINs. Meanwhile, [26] proposes a position-aware routing protocol for airborne mesh networks to efficiently mitigate threats from wormhole and blackhole attacks. Furthermore, [17] propose a secure, energy-efficient UAV relay framework using collaborative beamforming to jointly enhance secrecy and reduce propulsion energy consumption. Additionally, [18] analyzes security–reliability trade-offs in satellite–terrestrial relay networks with imperfect CSI by introducing a friendly jammer, deriving closed-form expressions for outage and intercept probabilities. [27] designs secure relay selection and user scheduling for hybrid satellite–terrestrial relay networks, deriving closed-form expressions for average secrecy capacity.

These studies have enabled secure communication over broader geographic areas through multi-hop relaying. However, these studies may not achieve optimal network utility as they adopted physical channels for routing, or do not consider the trade-off between transmission and jamming power. Thus, a cross-layer design to jointly optimize RRM and relay routing is required in multi-hop SAGSINs.

B. Notations and Variables

All variables adopted in the paper can be summarized in the below table.

Table 3. Summary of Notations.

Symbol	Description
Sets and Indices	
$\mathcal{M}$	Set of indices for Eves.
$\mathcal{I}$	Set of indices for network nodes, $\{0, 1, ..., I\}$.
$\mathcal{U}$	Set of indices for users, $\{1, ..., U\}$.
$\mathcal{N}$	Set of nodes and users in the graph $\mathcal{G}$.
$\mathcal{E}$	Set of edges in the graph $\mathcal{G}$.
$\mathcal{E}_u$	Set of edges in the relay path for user u.
S	A subset of nodes for the spanning tree constraint.
Physical Layer Parameters	
λ_i	Density of Eves in the network layer i.
$\boldsymbol{p}_i, \boldsymbol{p}_e$	Position vector of node i and Eve e.
$d^{\mathsf{s}}_{(i,j)}$	Distance between node i and node j.
$d^{\mathsf{e}}_{i,e}$	Distance between node i and Eve e.
α_i	Path loss exponent for the link from node i.
$h^{\mathsf{s}}_{(i,j)}, h^{\mathsf{e}}_{i,e}$	Small-scale Rayleigh fading channel coefficient for the legitimate link (i,j) and the wiretap link (i,e).
ρ_i	Transmit power density of node i.
σ_i	Jamming power density of node i.
n_0	Noise power spectral density.
$P_i^{\max}, P_i^{\min}$	Max/min transmission power of a node i.
$\beta_{(i,j),u}$	Bandwidth allocated to user u on the link (i,j).
Performance Metrics	
$\mathrm{SNR}^{\mathsf{s}}_{(i,j)}$	SNR of the legitimate link (i,j).
$\mathrm{SNR}^{\mathsf{e}}_{(i,e)}$	SNR of the wiretap link (i,e).
$C_{(i,j)}$	Secrecy capacity of the link (i,j).
$\mathbb{P}_{(i,j)}$	SPSC Probability for the link (i,j).
$\gamma_{(i,j)}$	Spectral efficiency of the link (i,j).
η_u	Relay throughput for user u.
h_u	Number of hops in the relay path for user u.
Graph and Routing Variables	
$\mathcal{G}_{\text{all}}$	Directed network routing graph.
$x_{(i,j)}$	Binary variable indicating if edge (i,j) is in the graph $\mathcal{G}$.
$x_{(i,j),u}$	Binary variable indicating if edge (i,j) is in the relay path $\mathcal{E}_u$ for user u.

C. Approximation of Ergodic Spectral Efficiency

We approximate the ergodic spectral efficiency to capture long-term network throughput. By Jensen's inequality, this approximation provides an upper bound on the ergodic spectral efficiency. Figure 12 validates the approximation by comparing the ergodic spectral efficiency with its no-fading counterpart. Over SNRs in the range [-40, 30] dB, the approximation closely matches the true curve in the low-SNR regime, and the gap widens as SNR increases. This gap can be reduced by introducing a scaling factor α that multiplies (9). A least-squares fit yields $\alpha = 0.8908$, achieving a mean squared error (MSE) of 0.008 over the specified SNR range. Hence, the approximation in (9) does not materially affect the decision variables, and any residual bias can be compensated by this simple linear rescaling.

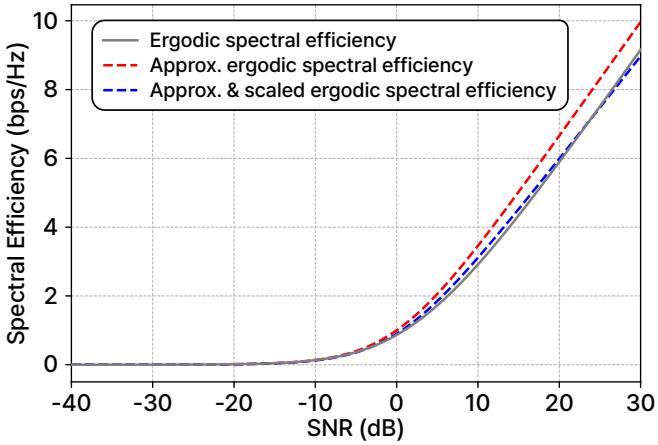

Fig. 12. Comparision between ergodic spectral effieciency and its approximation.

D. Derivation of the SPSC Probability

Using $|h^{\mathsf{e}}_{(i,e)}|^2 \sim \mathsf{Exp}(1)$, (15) can be simplified as follows:

$$\mathbb{P}_{(i,j)} = \mathbb{E}_{|h|^2}\Big[\exp\Big[-\lambda_i \int_{\mathbb{R}^2} \mathbb{P}\big(\mathrm{SNR}^{\mathsf{s}}_{(i,j)} < \mathrm{SNR}^{\mathsf{e}}_{(i,e)}\big)\, d\boldsymbol{p}_e\Big]\Big] \tag{37}$$

$$= \mathbb{E}_{|h|^2}\Big[\exp\Big[-\lambda_i \int_{\mathbb{R}^2} \mathbb{P}\Big(\frac{|h^{\mathsf{s}}_{(i,j)}|^2 (d^{\mathsf{e}}_{(i,e)})^{\alpha_i} n_0}{(d^{\mathsf{s}}_{(i,j)})^{\alpha_i} n_0 - \sigma_i G_{(i,j)} |h^{\mathsf{s}}_{(i,j)}|^2} < |h^{\mathsf{e}}_{(i,e)}|^2\Big) d\boldsymbol{p}_e\Big]\Big] \tag{38}$$

$$= \mathbb{E}_{|h|^2}\Big[\exp\Big[-\lambda_i \underbrace{\int_{\mathbb{R}^2} \exp\Big(-\frac{|h^{\mathsf{s}}_{(i,j)}|^2 (d^{\mathsf{e}}_{(i,e)} n_0)^{\alpha_i}}{(d^{\mathsf{s}}_{(i,j)})^{\alpha_i} n_0 - \sigma_i G_{(i,j)} |h^{\mathsf{s}}_{(i,j)}|^2}\Big) d\boldsymbol{p}_e}_{\textbf{(b)}}\Big]\Big]. \tag{39}$$

Then, we can apply a polar coordinate transform to (a), which give a direct integral as

$$\textbf{(b)} = \int_{\mathbb{R}^2} \exp\Big(-\frac{|h^{\mathsf{s}}_{(i,j)}|^2 (d^{\mathsf{e}}_{(i,e)} n_0)^{\alpha_i}}{(d^{\mathsf{s}}_{(i,j)})^{\alpha_i} n_0 - \sigma_i G_{(i,j)} |h^{\mathsf{s}}_{(i,j)}|^2}\Big) d\boldsymbol{p}_e \tag{40}$$

$$= \int_0^\infty r \exp\Big(-\frac{|h^{\mathsf{s}}_{(i,j)}|^2 r^{\alpha_i} n_0}{(d^{\mathsf{s}}_{(i,j)})^{\alpha_i} n_0 - \sigma_i G_{(i,j)} |h^{\mathsf{s}}_{(i,j)}|^2}\Big) dr \tag{41}$$

$$= \frac{2\pi}{\alpha_i}\Gamma\Big(\frac{2}{\alpha_i}\Big)\Big(-\frac{|h^{\mathsf{s}}_{(i,j)}|^2 n_0}{(d^{\mathsf{s}}_{(i,j)})^{\alpha_i} n_0 - \sigma_i G_{(i,j)} |h^{\mathsf{s}}_{(i,j)}|^2}\Big)^{-\frac{2}{\alpha_i}} \tag{42}$$

$$= \frac{2\pi}{\alpha_i}\Gamma\Big(\frac{2}{\alpha_i}\Big)(d^{\mathsf{s}}_{(i,j)})^2\Big(\frac{|h^{\mathsf{s}}_{(i,j)}|^2}{1 - \frac{\sigma_i G_{(i,j)}}{(d^{\mathsf{s}}_{(i,j)})^{\alpha_i} n_0} |h^{\mathsf{s}}_{(i,j)}|^2}\Big)^{-\frac{2}{\alpha_i}}. \tag{43}$$

Plugging in (b) into (39) and applying Jensen's inequality gives

$$\mathbb{P}_{(i,j)} \approx \exp\big[\mathbb{E}_{|h|^2}[\textbf{(b)}]\big] \tag{44}$$

$$= \exp\Big[-\lambda_i \frac{2\pi}{\alpha_i}\Gamma\Big(\frac{2}{\alpha_i}\Big)(d^{\mathsf{s}}_{(i,j)})^2 \underbrace{\mathbb{E}_{|h|^2}\Big[\Big(\frac{|h^{\mathsf{s}}_{(i,j)}|^2}{1 - \frac{\sigma_i G_{(i,j)}}{(d^{\mathsf{s}}_{(i,j)})^{\alpha_i} n_0} |h^{\mathsf{s}}_{(i,j)}|^2}\Big)^{-\frac{2}{\alpha_i}}\Big]}_{\textbf{(c)}}\Big] \tag{45}$$

Finally, applying the binomial approximation on the denominator of (b) results in

$$\textbf{(c)} = \mathbb{E}_{|h|^2}\Big[|h^{\mathsf{s}}_{(i,j)}|^{-\frac{4}{\alpha_i}}\Big(1 - \frac{\sigma_i G_{(i,j)}}{(d^{\mathsf{s}}_{(i,j)})^{\alpha_i} n_0} |h^{\mathsf{s}}_{(i,j)}|^2\Big)^{\frac{2}{\alpha_i}}\Big]$$

$$\approx \mathbb{E}_{|h|^2}\Big[|h^{\mathsf{s}}_{(i,j)}|^{-\frac{4}{\alpha_i}}\Big(1 - \frac{2\sigma_i G_{(i,j)}}{\alpha_i (d^{\mathsf{s}}_{(i,j)})^{\alpha_i} n_0} |h^{\mathsf{s}}_{(i,j)}|^2\Big)\Big]$$

$$= \mathbb{E}_{|h|^2}\big[|h^{\mathsf{s}}_{(i,j)}|^{-\frac{4}{\alpha_i}}\big] - \frac{2\sigma_i G_{(i,j)}}{\alpha_i (d^{\mathsf{s}}_{(i,j)})^{\alpha_i} n_0}\mathbb{E}_{|h|^2}\Big[|h^{\mathsf{s}}_{(i,j)}|^{2-\frac{4}{\alpha_i}}\Big]$$

$$= \Gamma\big(1 - \frac{2}{\alpha_i}\big) - \frac{2\sigma_i G_{(i,j)}}{\alpha_i (d^{\mathsf{s}}_{(i,j)})^{\alpha_i} n_0}\Gamma\big(2 - \frac{2}{\alpha_i}\big) \tag{46}$$

Then, the SPSC probabilty can be approximately derived as

$$\mathbb{P}_{(i,j)} = \exp\Big[-\kappa_i\Big[\Gamma\big(1 - \frac{2}{\alpha_i}\big) - \frac{2\sigma_i G_{(i,j)}}{\alpha_i (d^{\mathsf{s}}_{(i,j)})^{\alpha_i} n_0}\Gamma\big(2 - \frac{2}{\alpha_i}\big)\Big](d^{\mathsf{s}}_{(i,j)})^2\Big] \tag{47}$$

for $\kappa_i = \lambda_i \frac{2\pi}{\alpha_i}\Gamma(\frac{2}{\alpha_i})$. When $\sigma_i = 0$, this approximation reduces to the previously reported result in [28], demonstrating both the validity and extensibility of the derivation.

E. Derivation of the Bound Gap in the SPSC Approximation

E.1. High Pathloss Exponent Case

For brevity of notations, we define

$$\Phi(|h|^2) := \frac{2\pi}{\alpha_i}\Gamma(\frac{2}{\alpha_i})(d^{\mathsf{s}}_{(i,j)})^2\left(\frac{|h|^2}{1-\frac{\sigma_i G_{(i,j)}}{(d^{\mathsf{s}}_{(i,j)})^{\alpha_i} n_0}|h|^2}\right)^{-\frac{2}{\alpha_i}} \tag{48}$$

which is a non-negative random variable depending on the fading coefficient $|h|^2 \sim \exp(1)$. With this notation, the original success probability is written as

$$\mathbb{P}_{(i,j)} = \mathbb{E}_{|h|^2}\left[\exp(-\lambda_i \Phi(h))\right]. \tag{49}$$

Since the exponential function is convex, Jensen's inequality yields

$$\mathbb{E}_{|h|^2}\left[\exp(-\lambda_i \Phi(|h|^2))\right] \geq \tilde{\mathbb{P}}_{(i,j)} := \exp\left(-\lambda_i \mu\right), \tag{50}$$

for $\mu := \mathbb{E}_{|h|^2}[\Phi(|h|^2)]$.

Define the Jensen gap as

$$\Delta := \mathbb{P}_{(i,j)} - \tilde{\mathbb{P}}_{(i,j)} \geq 0. \tag{51}$$

Let $\varphi(x) = e^{-\lambda_i x}$, which is convex on $[0,\infty)$ with $\varphi''(x) = \lambda_i^2 e^{-\lambda_i x} \leq \lambda_i^2$. A standard bound on Jensen gaps for convex functions yields

$$0 \leq \Delta = \mathbb{E}_h[\varphi(\Phi)] - \varphi(\mu) \tag{52}$$

$$\leq \frac{1}{2}\sup_{x\geq 0}\varphi''(x)\mathrm{Var}(\Phi) \leq \frac{\lambda_i^2}{2}\mathrm{Var}(\Phi). \tag{53}$$

The bound in (53) holds whenever $\mathrm{Var}(\Phi) < \infty$.

For any m with $\frac{2m}{\alpha_i} < 1$, the m-th moment exists and equals

$$\mathbb{E}\left[\Phi^m\right] = \left(\frac{2\pi}{\alpha_i}\Gamma(\frac{2}{\alpha_i})(d^{\mathsf{s}}_{(i,j)})^2\right)^m\left(\frac{|h|^2}{1-\frac{\sigma_i G_{(i,j)}}{(d^{\mathsf{s}}_{(i,j)})^{\alpha_i} n_0}|h|^2}\right)^{-\frac{2m}{\alpha_i}} \tag{54}$$

$$= \left(\frac{2\pi}{\alpha_i}\Gamma(\frac{2}{\alpha_i})(d^{\mathsf{s}}_{(i,j)})^2\right)^m\left[\Gamma\big(1-\frac{2m}{\alpha_i}\big) - \frac{2m\sigma_i G_{(i,j)}}{\alpha_i (d^{\mathsf{s}}_{(i,j)})^{\alpha_i} n_0}\Gamma\big(2-\frac{2m}{\alpha_i}\big)\right] \tag{55}$$

Then, we have

$$\mu = \frac{2\pi}{\alpha_i}\Gamma(\frac{2}{\alpha_i})(d^{\mathsf{s}}_{(i,j)})^2\left[\Gamma\big(1-\frac{2}{\alpha_i}\big) - \frac{2\sigma_i G_{(i,j)}}{\alpha_i (d^{\mathsf{s}}_{(i,j)})^{\alpha_i} n_0}\Gamma\big(2-\frac{2}{\alpha_i}\big)\right] \tag{56}$$

$$\mathrm{Var}(\Phi) = \left(\frac{2\pi}{\alpha_i}\Gamma(\frac{2}{\alpha_i})(d^{\mathsf{s}}_{(i,j)})^2\right)^2\left[\Gamma\big(1-\frac{4}{\alpha_i}\big) - \frac{4\sigma_i G_{(i,j)}}{\alpha_i (d^{\mathsf{s}}_{(i,j)})^{\alpha_i} n_0}\Gamma\big(2-\frac{4}{\alpha_i}\big)\right]. \tag{57}$$

Plugging (57) in (53) provides a tight Jensen bound when $\alpha_i > 4$.

E.2. Low Pathloss Exponent Case

When $\alpha_i < 4$, the variance of Φ diverges since the integral (43) assumes that Eves are distributed over an infinitely large space. Instead, we restrict the integration domain to $(0, R)$ to compute a more accurate gap. As Δ increases with α_i, (53) is bounded by $\mathrm{Var}(\Phi)$ at $\alpha_i = 4$.

Then, for $C = \left[(d^{\mathsf{s}}_{(i,j)})^{\alpha_i} n_0 - \sigma_i G_{(i,j)}|h^{\mathsf{s}}_{(i,j)}|^2\right]^{-1}$, we have

$$\mathbb{E}_{|h|^2}[\Phi] = 2\pi\int_0^R r\mathbb{E}_{|h|^2}\left[\exp\left(-C|h|^2 r^4\right)\right]dr \tag{58}$$

$$= \pi\int_0^R \frac{r}{1+Cr^4}dr \tag{59}$$

$$= \frac{\pi}{\sqrt{C}} \arctan(R^2\sqrt{C}) \approx \frac{\pi^2}{2\sqrt{C}} \tag{60}$$

for sufficiently large R.

Also, for variance, we have

$$\mathbb{E}_{|h|^2}[\Phi^2] = \mathbb{E}_{|h|^2}\left[\left(2\pi \int_0^R r \exp\left(-C|h|^2 r^4\right) dr\right)^2\right] \tag{61}$$

$$= \pi^2 \int_0^{R^2}\int_0^{R^2} \mathbb{E}_{|h|^2}\Big[\exp\left(-C|h|^2(u^2+s^2)\right)\Big] duds \tag{62}$$

$$= \pi^2 \int_0^{R^2}\int_0^{R^2} \frac{duds}{1+C(r_1^4+r_2^4)} \tag{63}$$

$$\leq \pi^2 \int_0^{2\pi}\int_0^{\sqrt{2}R^2} \frac{r}{1+Cr^2} dr d\theta \tag{64}$$

$$= \frac{\pi^3}{4C} \ln(1+2CR^4) \approx \frac{\pi^2}{C} \ln R. \tag{65}$$

Thus, we have

$$\text{Var}(\Phi) = \frac{\pi^3}{C} \ln R - \frac{\pi^4}{4C}. \tag{66}$$

Then, plugging (66) in (53) provides an asymptotic bound for $\alpha_i < 4$.

F. Visualization of the MCRR Algorithm

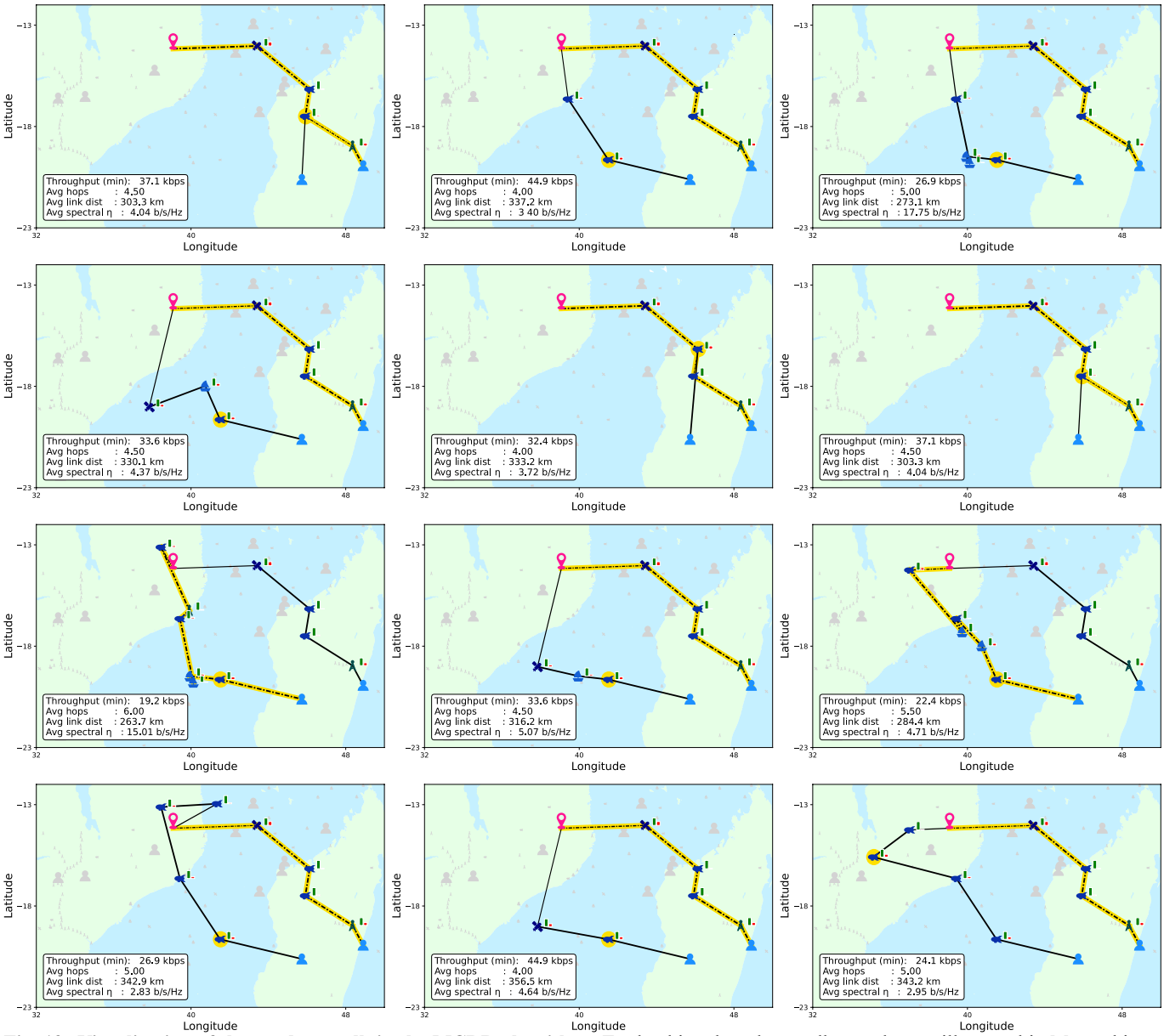

Fig. 13. Visualization of the random-walk in the MCRR algorithm. Twelve biased random walk samples are illustrated in Mozambique-Madagascar testbed. Among them, a path with the largest min throughput is selected for the user. The highlighted dashed line represents the longest path. The highlighted node represents the min-throughput node.

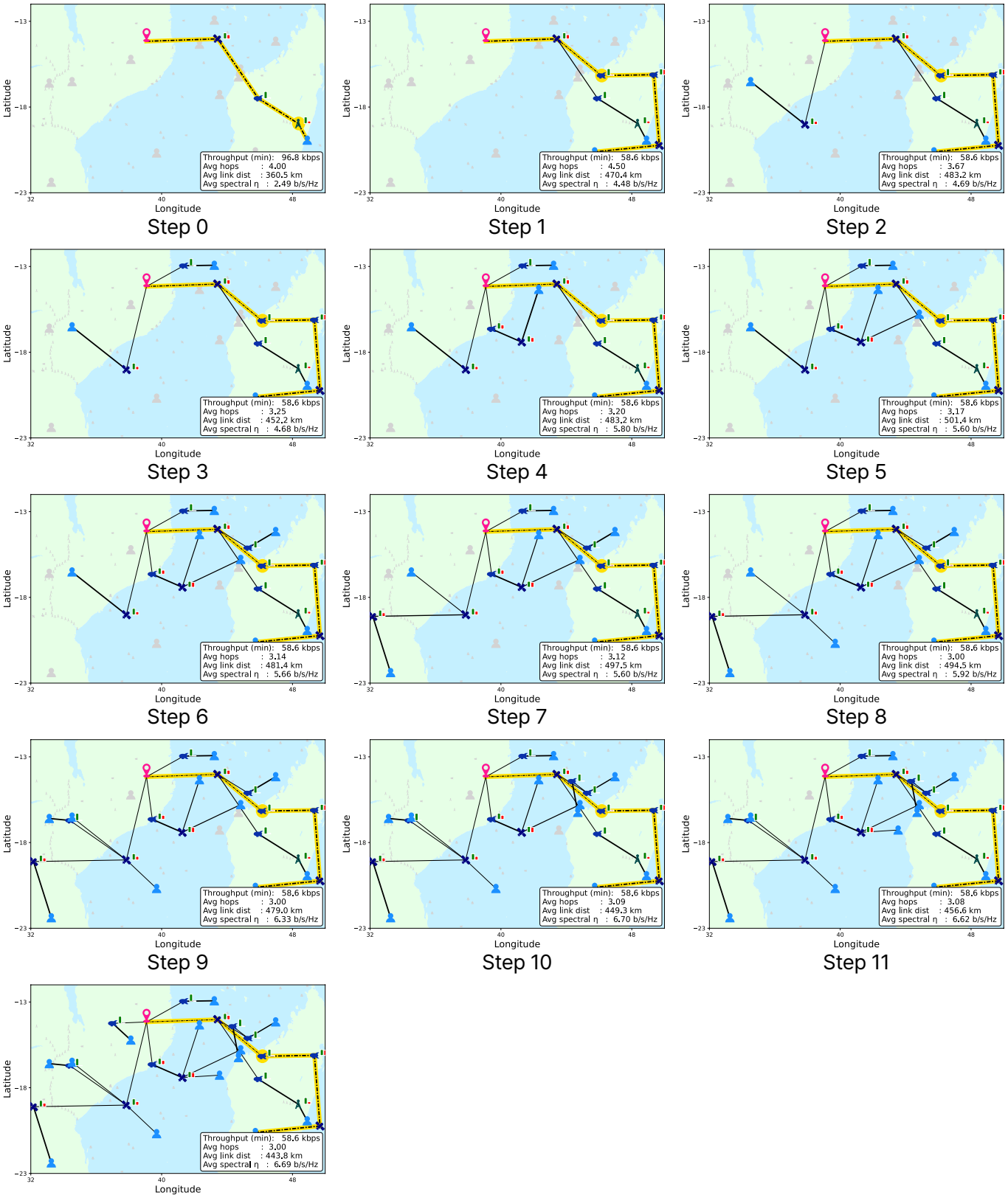

Fig. 14. Step-by-step visualization of the MCRR algorithm implemented in Mozambique-Madagascar testbed. The highlighted dashed line represents the longest path. The highlighted node represents the min-throughput node.